scientific reports

Check for updates

OPEN

Effect of bed clay on surface water-wave reconstruction from ripples

Jonathan Malarkey[1]✉, Ellen M. Pollard[2], Roberto Fernández[3], Xuxu Wu[2,4], Jaco H. Baas[1] & Daniel R. Parsons[5]

Wave ripples can provide valuable information on their formative hydrodynamic conditions in past subaqueous environments by inverting dimension predictors. However, these inversions do not usually take the mixed non-cohesive/cohesive nature of sediment beds into account. Recent experiments involving sand–kaolinite mixtures have demonstrated that wave-ripple dimensions and the threshold of motion are affected by bed clay content. Here, a clean-sand method to determine wave climate from orbital ripple wavelength has been adapted to include the effect of clay and a consistent shear-stress threshold parameterisation. From present-day examples with known wave conditions, the results show that the largest clay effect occurs for coarse sand with median grain diameters over 0.45 mm. For a 7.4% volumetric clay concentration, the range of possible water-surface wavelengths and water depths can be reduced significantly, by factors of three and four compared to clean sand, indicating that neglecting clay when present will underestimate the wave climate.

Keywords Geology, Oceanography, Sediment transport, Sand-clay mixtures, Wave reconstruction, Wave ripples

Bed-surface structures in sediments and sedimentary rocks of past subaqueous environments provide important information on flow hydraulics[1]. These structures tend to be classified on the basis of the presence or absence of cohesion in equivalent modern environments: (a) cohesive structures, associated with physical cohesion by clay particles and biological cohesion by extracellular polymeric substances (EPS), e.g. biofilms[2], where the bed is stabilised by cohesion between grains and sudden catastrophic failure may occur under high bed shear stress, e.g. during storms; and (b) non-cohesive bedforms (e.g. wave and current ripples[3,4]), where grains can move individually and tend to respond more rapidly and continuously to changes in flow forcing[5]. Examples of these types of bed-surface structure include roll-ups[6] and non-cohesive wave ripples[7]. Davies et al.[8] argued that the distinction between cohesive and non-cohesive sedimentary structures is artificial, as they represent end members of a spectrum, and thus predictions based on one classification may result in misinterpretations. This position is re-enforced by recent experiments that have shown how sandy bedforms can be affected by small amounts of biological and physical cohesion[9–12]. The consequence for wave ripples of physical cohesion associated with kaolin clay in the bed has been detailed by Wu et al.[13]. Building on previous work[7], Diem[14] developed a clean-sand analytical method for the prediction of paleowave climate based on the dimensional measurement of wave ripples in the rock record[15–19]. Here, the Diem[14] approach is adapted for sand–clay mixtures, using the synthesis proposed by Wu et al.[13].

The Diem[14] approach starts by determining the wave orbital diameter from the ripple wavelength, without requiring a specific wavelength predictor. Here, the formulation starts as Diem[14] did, with linear wave theory and additional constraints based on threshold of motion and wave breaking. It will then return to the effect of clay on ripple-wavelength prediction and the threshold of motion. Since wave conditions from the rock record are unknown, the importance of clay content is demonstrated with the use of present-day examples from the laboratory and field, where the wave conditions were known.

Results

The Diem[14] approach

Wave conditions

Based on linear wave theory, the Diem[14] approach uses expressions for the dispersion relation and the wave-velocity amplitude, U_0, together with conditions for the threshold of motion and wave breaking, to give

[1]School of Ocean Sciences, Bangor University, Menai Bridge, Anglesey LL59 5AB, UK. [2]Energy and Environment Institute, University of Hull, Hull HU6 7RX, UK. [3]Department of Civil and Environmental Engineering, The Pennsylvania State University, University Park, PA 16802, USA. [4]School of Ocean and Earth Science, University of Southampton, Southampton SO14 3ZH, UK. [5]Department of Geography and Environment, Loughborough University, Loughborough LE11 3TU, UK. ✉email: j.malarkey@bangor.ac.uk

$$x < \tanh kh, \tag{1a}$$

$$x \geqslant A\cosh kh, \tag{1b}$$

(see "Methods") where $x = L/L_{t\infty}$, L is the water-surface wavelength, $L_{t\infty} = \pi g(d_0/U_t)^2/2$ is the deep-water surface wavelength corresponding to the threshold of motion, $k = 2\pi/L$, h is the water depth, g is the acceleration due to gravity ($= 9.81$ m s^2), d_0 is the orbital diameter ($= H/\sinh kh$, H is the wave height), U_t is the critical wave-velocity amplitude associated with the threshold of motion and $A = d_0/0.142L_{t\infty}$. As will be seen later, U_t is a function of d_0 and D_{50}, the median grain diameter, and A can be defined as $(U_t/U_m)^2/2$, where $U_m = (0.0355\pi g d_0)^{1/2}$ is the maximum wave-velocity amplitude. Since wave-velocity amplitude and orbital diameter are related by $U_0 = \pi d_0/T$, where T is the wave period, U_0 and T are in the ranges $U_t < U_0 \leq U_m$ and $\pi d_0/U_m \leq T < \pi d_0/U_t$.

Equation (1a, b) represent the range of possible conditions between threshold and wave breaking for the wave climate, such that x is in the range $A\cosh kh \leq x < \tanh kh$, and $A < 1/2$ for there to be any allowable conditions (see "Methods"). Figure 1 shows kh versus x for the limiting single-valued $A = 1/2$ case ($U_m^2 = U_t^2$) from shallow water ($kh \ll 1$) to deep water ($kh \gg 1$). Figure 1 also shows the $A = 1/4$ case ($U_m^2 = 2U_t^2$), corresponding to typical above-threshold wave conditions. In the latter case, the shaded region in Fig. 1 shows the allowable values of x [the "Methods" section explains how intersection points, (x_{min}, kh_{min}) and (x_{max}, kh_{max}), are determined]. The breaking-wave curves ($x = A\cosh kh$) are concave downward and the threshold curve ($x = \tanh kh$) is concave upward. Notice for the breaking-wave curves, $x \to A$ for $kh \ll 1$ and A also controls the slope for larger kh. In dimensional terms, L is therefore limited by the threshold scale ($L_{t\infty}$) and breaking-wave scale ($AL_{t\infty}$) according to $AL_{t\infty} < L \leq L_{t\infty}$. Then, from equations (1a, b), the range of h can be expressed as a function of L as.

$$(L/2\pi)\operatorname{arctanh}(L/L_{t\infty}) < h \leqslant (L/2\pi)\operatorname{arccosh}(L/AL_{t\infty}) \tag{2}$$

The ripple predictor

Diem's[14] central assumption is that the orbital diameter can be expressed in terms of a ripple wavelength, which is assumed to be in equilibrium, λ_e, as

$$\lambda_e = \alpha_0 d_0, \tag{3}$$

where $\alpha_0 = 0.65$, based on the experiments[20], provided that $\lambda_e < 200$ mm ($d_0 = 308$ mm). Above this limit, Diem[14] used the Sleath[21] predictor. This arbitrary 200-mm limit represents the lower boundary of the suborbital and anorbital ranges, where the wavelength is dependent on both d_0 and D_{50} for suborbital ripples and only dependent on D_{50} for anorbital ripples. However, while a value of α_0 in the range $0.5 \leq \alpha_0 \leq 0.75$ in Eq. (3) is widely accepted, there is little agreement in the literature on the precise nature of the orbital, suborbital, and anorbital limits[22].

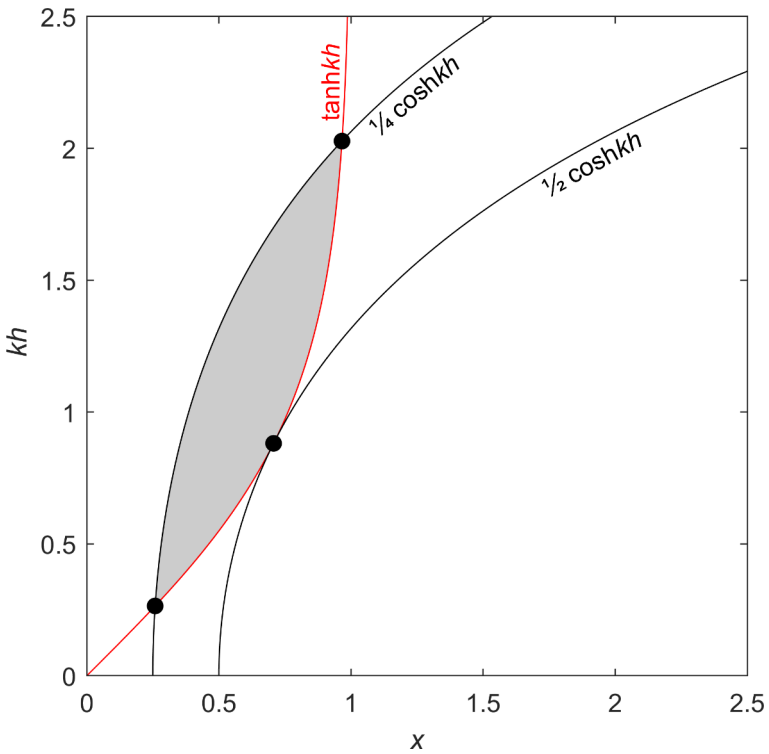

Fig. 1. kh versus x ($L/L_{t\infty}$) for the limiting case of $A = 1/2$ and also $A = 1/4$. The dots correspond to $x = 2^{-1/2}$ and $kh = \operatorname{arctanh} 2^{-1/2}$, for $A = 1/2$; $x_{max,\,min} = (2 \pm 3^{1/2})^{1/2}/2$ and $kh_{max,\,min} = \operatorname{arctanh}[x_{max,\,min}]$, for $A = 1/4$ (see "Methods", Eq. (9)), and shading represents allowable values of x and kh for $A = 1/4$ ($A\cosh kh \leq x < \tanh kh$).

Wiberg and Harris[3] defined orbital, suborbital and anorbital ripples by $d_0/D_{50} \leq 1754$, $1754 < d_0/D_{50} \leq 5587$ and $d_0/D_{50} > 5587$, respectively[23], whereas other researchers have argued the anorbital limit should have wave-period dependence[24,25]. Provided that Eq. (3) *does* hold, which is what will be assumed here, all quantities involving d_0 can now be expressed in terms of λ_e. Wu et al.[13], and other researchers previously[26,27], have demonstrated that d_0 can be modified by the presence of a current. However, as the method relies on there being a one-to-one correspondence between d_0 and λ_e, this effect cannot be included and so conditions must be restricted to waves in isolation.

Adaptions to the Diem[14] approach

Threshold of motion parameterisation

Based on the Soulsby[28] critical threshold of motion for clean sand, the "Methods" section derives an expression for U_t^2, Eq. (11), such that U_t^2, $L_{t\infty}$ and $AL_{t\infty}$ can be written

$$U_t{}^2 = B(g d_0{}^{0.52} D_{50}^{0.48}), \tag{4a}$$

$$L_{t\infty} = \frac{\pi d_0}{2B}\left(\frac{d_0}{D_{50}}\right)^{0.48}, \tag{4b}$$

$$AL_{t\infty} = \frac{d_0}{0.142}, \tag{4c}$$

where $B = 3.653(s-1)\theta_0$, s is the relative density of sediment in water, θ_0 is the critical skin friction Shields parameter, Eq. (10), and $d_0 = \lambda_e/\alpha_0$ from Eq. (3). Diem[14] used the Komar and Miller[29] mobility threshold prescription. Here, the Soulsby[28] expression has been used, as it allows U_t^2 to be directly related to θ_0 and it avoids the need for two different functional forms, for $D_{50} < 0.5$ mm and $D_{50} \geq 0.5$ mm (Eqs. (12) and (13)).

Inclusion of the effect of clay

Wu et al.[13] showed that the ratio of wavelength to orbital diameter, α, which replaces α_0 in Eq. (3), can be expressed as

$$\alpha = \alpha_0 \begin{cases} 1, & C_0 \leqslant C_{0m}, \\ 1 - 5.5(C_0 - C_{0m}), & C_0 > C_{0m}, \end{cases} \tag{5}$$

where α_0 is the clean-sand constant of proportionality ($=0.61$), C_0 is the clay content in the bed, $C_{0m} = 7.4\%$ is the minimum value of C_0 where α can change from α_0 and $\alpha = \alpha_0/2$ for $C_0 = 16.3\%$. Whitehouse et al.[30] showed that the threshold of motion is enhanced by the clay content according to

$$\theta_{0E} = \theta_0 B_\theta, \tag{6}$$

where θ_0 is the clean-sand threshold, $B_\theta = 1 + P_\theta C_0$ and P_θ is a constant that depends on the sediment properties. Based on their experiments, Wu et al.[13] determined that $P_\theta = 6.3$ for $D_{50} = 0.143$ mm and $P_\theta = 23$ for $0.45 \leq D_{50} \leq 0.5$ mm (between these two ranges, it will be assumed that P_θ can be linearly interpolated). Notice in Eq. (6) that even small amounts of clay produce an enhancement which is strongly dependent on grain size.

Thus, the two main effects of including clay are that α is reduced and θ_{0E} is increased. Substituting Eqs. (5) and (6), into Eqs. (4a, b, c) gives U_t^2, $L_{t\infty}$ and $AL_{t\infty}$ as

$$U_t{}^2 = B\left[\frac{B_\theta}{\alpha^{0.52}}\right](g\lambda_e^{0.52} D_{50}^{0.48}), \tag{7a}$$

$$L_{t\infty} = \frac{\pi\lambda_e}{2B[B_\theta \alpha^{1.48}]}\left(\frac{\lambda_e}{D_{50}}\right)^{0.48}, \tag{7b}$$

$$AL_{t\infty} = \frac{\lambda_e}{0.142[\alpha]}, \tag{7c}$$

where λ_e is the mixed clay–sand ripple wavelength and only the square-bracketed quantity in each expression depends on C_0.

The adapted procedure

The procedure begins with the determination of the ripple wavelength, λ_e, and bed-clay content, C_0. Once these have been determined, the following calculations are undertaken:

(i) Use λ_e and C_0 in equations (7a, b,c), with α and B_θ given by Eqs. (5) and (6), to determine U_t, $L_{t\infty}$ and $AL_{t\infty}$
(ii) Use A in Eq. (9) to determine $x_{max,\,min}$, so that $x_{min} \leq x \leq x_{max}$
(iii) Use $L = L_{t\infty}x$ to determine the range of h based on Eq. (2) and U_t and $U_m = (0.0355\pi g\lambda_e/\alpha)^{1/2}$ to determine the ranges of U_0 and T: $U_t < U_0 < U_m$ and $\pi\lambda_e/\alpha U_m < T < \pi\lambda_e/\alpha U_t$

Example cases

With specific examples from the rock record, Diem[14] was able to show how local considerations and context could be used to further limit the theoretical ranges described in the previous section. Here, modern-day

examples, where the wave properties are known, are used, so that attention can be focussed on the effect of clay on the theoretical ranges alone. The example cases correspond to clean, coarse-, medium- and fine-grained sand from the laboratory and field, and involve determining how wave conditions based on the measured ripples change if the clay content is varied in the range $0 \le C_0 \le 16.3\%$.

Wu et al.[11], coarse-sand laboratory data

Wu et al.[11] conducted a series of experiments involving a single-wave condition over a bed composed of well-sorted coarse sand, $D_{50} = 0.496$ mm ($\theta_0 = 0.032$), and varying clay content, $0 \le C_0 \le 7.4\%$. For the clean sand experiment ($C_0 = 0\%$), the wave conditions were given by $h = 0.6$ m, $H = 0.16$ m and $T = 2.49$ s ($L = 5.62$ m), corresponding to $d_0 = 0.223$ m. Despite the coarse grain size, which allowed clay and sand particles to be distinguished more readily in the experiments, Wu et al.[12] demonstrated that these hydrodynamic conditions were comparable to an intertidal site in the macrotidal Dee Estuary with a medium grain size[31]. This experiment produced ripples with a wavelength $\lambda_e = 278 D_{50}$[13]. Figure 2a shows the threshold and wave-breaking scales, $L_{t\infty}$ and $AL_{t\infty}$, versus C_0. $L_{t\infty}$, which is smallest at $C_0 = 7.4\%$, has a much larger range than $AL_{t\infty}$, which is constant for $C_0 \le 7.4\%$ and then doubles up to $C_0 = 16.3\%$. Figure 2d shows the corresponding L-h phase space, based on Eq. (2), for the clay contents depicted in Fig. 2a ($C_0 = 0$, 7.4 and 16.3%). Compared to the dimensionless x–kh plot (Fig. 1), the threshold curves are still concave downwards, but more exaggerated, and the breaking-wave curves are close to straight lines. The change in ranges is largely due to changes in $L_{t\infty}$. The reduction in range between the largest and smallest (corresponding to $C_0 = 0\%$ and 7.4%) is by a factor of 3 and 4 for the water-surface wavelength and water depth, respectively (Fig. 2d). Notice that the actual surface wavelength and water depth ($L = 5.62$ m, $h = 0.6$ m) are within all three ranges. Figure 2a, d can be compared with Fig. 4a, b to see the effect of using the Komar and Miller[29] clean-sand mobility description for the threshold. This shows $L_{t\infty}$ to be about 63% of its value in Fig. 2a, because $B = 0.21(s-1) = 0.34$ as opposed to $3.653(s-1)\theta_0 = 0.19$. Thus, using the Diem[14] clean-sand mobility description underpredicts the range of water-surface wavelengths and heights in an absolute sense. In a relative sense, the change in the ranges with clay content is similar, because the powers of d_0 and D_{50} are similar (Eq. (13), for $D_{50} < 0.5$ mm, and Eq. (7a)), but this will not be the case for $D_{50} > 0.5$ mm. Also,

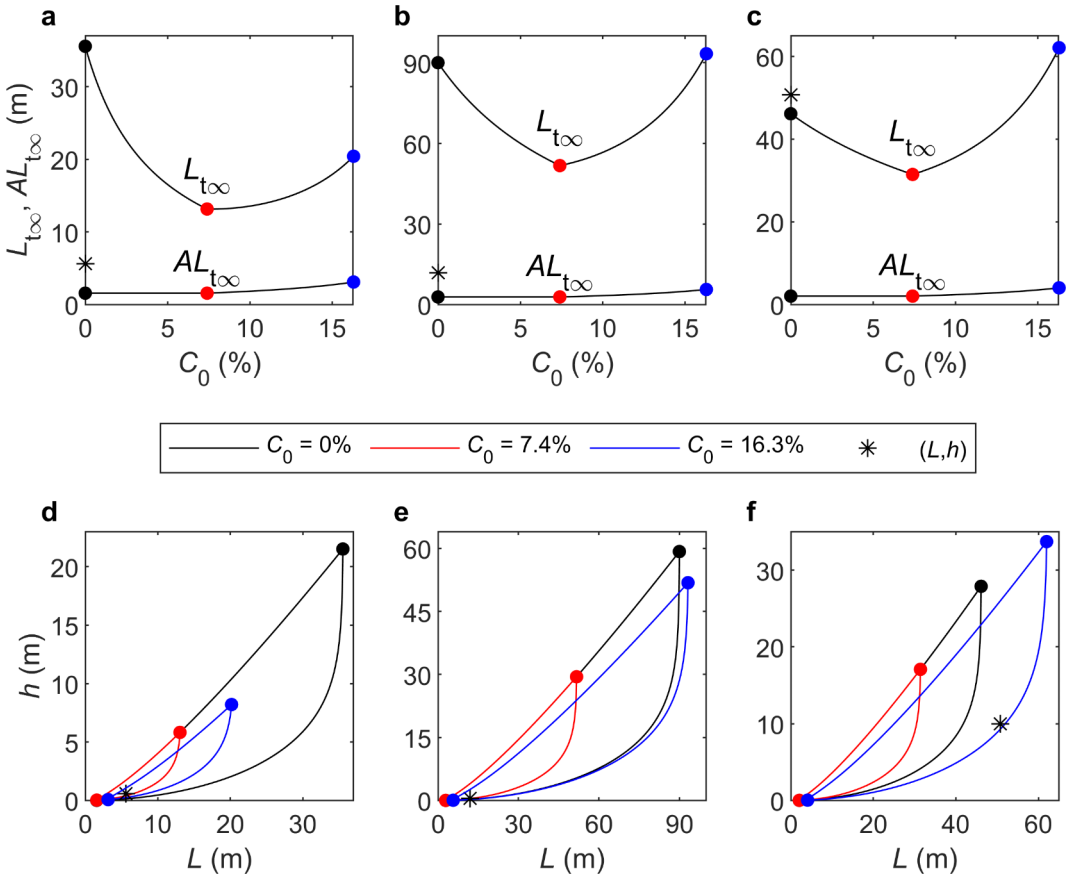

Fig. 2. (**a**–**c**) Threshold, $L_{t\infty}$, and wave-breaking, $AL_{t\infty}$, scales, equations (7b, c), versus C_0 and (**d**–**f**) L–h phase space from Eq. (2), showing the different ranges for $C_0 = 0$, 7.4 and 16.3% and the measured L and h. For (**a**,**d**) Wu et al.[11], $\lambda_e = 278 D_{50}$, $D_{50} = 0.496$ mm, $\theta_0 = 0.032$, $L = 5.62$ m and $h = 0.6$ m; for (**b**,**e**) Doucette[32], $\lambda_e = 250$ mm, $D_{50} = 0.22$ mm, $\theta_0 = 0.045$, $L = 11.9$ m and $h = 0.47$ m, and for (**c**,**f**) Boyd et al.[33], $\lambda_e = 180$ mm, $D_{50} = 0.11$ mm, $\theta_0 = 0.076$, $L = 50.7$ m and $h = 10$ m. Legend applies to (**d**–**f**); colours in (**a**–**c**) are consistent with the legend.

the measured L and h are not within the $C_0 = 7.4\%$ range (Fig. 4b). As L and h are below the threshold curve, this would imply that ripples of this size are relict for this clay content. This is inconsistent with the experimental results, since Wu et al.[13] showed no reduction in λ_e for $C_0 \leq 7.4\%$.

Doucette[32], medium-sand field data

The Doucette[32] field measurements were taken on a microtidal beach of Wambro Sound, Western Australia, near Perth (run 1) where $h = 0.47$ m, $H = 0.2$ m and $T = 5.6$ s ($L = 11.9$ m), corresponding to $d_0 = 0.79$ m. The bed was composed of medium sand, with $D_{50} = 0.22$ mm ($\theta_0 = 0.045$), and the measured ripples had a wavelength of $\lambda_e = 250$ mm. This example case builds on the Wu et al.[11] example case by corresponding to both the hydrodynamics and medium grain size of the Dee Estuary UK[31]. Since $d_0/D_{50} = 3591$, the ripples were in the suborbital range, where the wavelength is dependent on both the orbital and grain diameters. Notice this wavelength is above Diem's[14] 200-mm limit. The methods section demonstrates that, whilst using the Sleath[21] predictor for $C_0 = 0$ produces a difference, it is similar to the other two example cases, which are below the Diem[14] limit, and so is not considered significant. From interpolation, P_θ in equation (6) is determined to be 10. Figure 2b shows $L_{t\infty}$ and $AL_{t\infty}$ versus C_0 and Fig. 2e shows the L–h phase space, for $C_0 = 0$, 7.4 and 16.3%. These reveal similar behaviour to that of the coarse-grained sand case, but less extreme: in Fig. 2b, $L_{t\infty}$ is still at its minimum at $C_0 = 7.4\%$ and $AL_{t\infty}$ shows the same enhancement as in Fig. 2a. The reduction in range between the largest and smallest ($C_0 = 0\%$ and 7.4%) is by a factor of 2 for both the water-surface wavelength and water depth (Fig. 2e). Again, the actual surface wavelength and water depth ($L = 11.9$ m, $h = 0.47$ m) are within all three ranges.

Boyd et al.[33], fine-sand field data

The Boyd et al.[33] field measurements were undertaken about 1 km from Martinique Beach on the Atlantic coast of Nova Scotia during a period of relative calm (day 167, hour 9) where $h = 10$ m, $H = 0.5$ m and $T = 6.2$ s ($L = 50.7$ m), corresponding to $d_0 = 0.32$ m. The bed was composed of well-sorted fine sand, with $D_{50} = 0.11$ mm ($\theta_0 = 0.076$), and the measured ripples had a wavelength of $\lambda_e = 180$ mm. Fine sands are common in many estuaries around the world, for example[34]. $d_0/D_{50} = 2873$ puts the ripples into the suborbital range. Assuming that Pθ in equation (6) is the same as for 0.143 mm ($P_\theta = 6.3$), Fig. 2c shows $L_{t\infty}$ and $AL_{t\infty}$ versus C_0 and Fig. 2f shows the L–h phase space, for $C_0 = 0$, 7.4 and 16.3%. $L_{t\infty}$ in Fig. 2c is still at its minimum at $C_0 = 7.4\%$, but, because of far weaker clay enhancement of the threshold for fine sands in equation (6), $L_{t\infty}$ is largest for $C_0 = 16.3\%$. In Fig. 2f, the measured water-surface wavelength and water depth ($L = 50.7$ m, $h = 10$ m) are below the threshold curve and outside the range for the $C_0 = 0$ and 7.4% clay contents, and just above the threshold curve and within range for $C_0 = 16.3\%$, because, unlike the previous cases, $C_0 = 16.3\%$ produces the largest $L_{t\infty}$. Since there was little clay at the field site, the wave conditions were probably below threshold, implying that the observed ripples were relict. This is supported by the fact that Boyd et al.'s[33] previous observation at day 167, hour 3, showed the same wavelength and no ripple migration. The reduction in range between the largest and smallest ($C_0 = 16.3\%$ and 7.4%) is again by a factor of 2 for both the water-surface wavelength and water depth (Fig. 2f).

Discussion

The range of L shown in Fig. 2 is largely controlled by $L_{t\infty}$, so it is of interest to determine how the change in clay content affects $L_{t\infty}$, Eq. (7b), compared to the original clean-sand Diem[14] method using Komar and Miller[29], $L_{t\infty KM}$, Eq. (13) with $C_0 = 0\%$. The net effect is shown as a ratio in Fig. 3 for $C_0 = 0$, 7.4 and 16.3% and $0.1 \leq D_{50} \leq 0.8$ mm, for the approximate limits in the range of λ_e/D_{50} of 250 and 1,000. There are two competing effects: the reduction because of clay content (Fig. 2) and the increase because of using the Soulsby[28] threshold condition rather than the Komar and Miller[29]. Figure 3 shows a discontinuity for clean sand at $D_{50} = 0.5$ mm as a result of Eq. (13), leading to the largest difference ($L_{t\infty}$ is increased by up to 161% for $\lambda_e/D_{50} = 250$), which decreases with increasing λ_e/D_{50} (although the Diem[14] method has rarely been applied for $D_{50} > 0.5$ mm). Otherwise for $D_{50} \leq 0.19$ mm, $L_{t\infty}$ is reduced by up to 36%, and for $0.19 < D_{50} \leq 0.5$ mm, $L_{t\infty}$ is increased by up to 64%. For $C_0 = 7.4\%$, $L_{t\infty}$ is consistently decreased by between 35 and 56%, and for $C_0 = 16.3\%$, $L_{t\infty}$ varies only slightly (increased by up to 14%, for $0.12 \leq D_{50} \leq 0.37$ mm, and otherwise reduced by up to 15%). The absence of a discontinuity in the present formulation, compared to Diem's[14] original formulation, is clearly preferable. Also, the net effect of the clay on $L_{t\infty}$ will be stronger for smaller than for larger clay contents. It should be remembered that the present method, like the original Diem[14] method, is only applicable to waves alone.

It is important to clarify how a representative clay content, C_0, for the ripples should be determined. In the modern environment this usually involves measuring C_0 below the active layer (below trough level), as efficient winnowing often removes clay from the body of the ripples during development[12]. In the geological record, where the method still requires testing, clay content in deposits should be based on primary clay minerals and diagenetic alterations for which it can be established that the original mineral was part of the primary clay fraction. The laboratory experiments used in this study[13] are based only on the physical cohesion associated with kaolin, and not the biological cohesion associated with EPS that often occur together with clay in the field[35]. Since, the effect of EPS can be quite substantial[2,9], the present method should be interpreted as a conservative estimate in the field. For instance, Baas et al.[35] concluded that ripple development in the field compared to the laboratory was significantly delayed due to the additional presence of EPS leading to a greater enhancement in the threshold of motion, see Eq. (6). EPS delaying development may also challenge the equilibrium wavelength assumption, see Eq. (3). Further study of the effects of combined clay and EPS on wave ripples is thus still required.

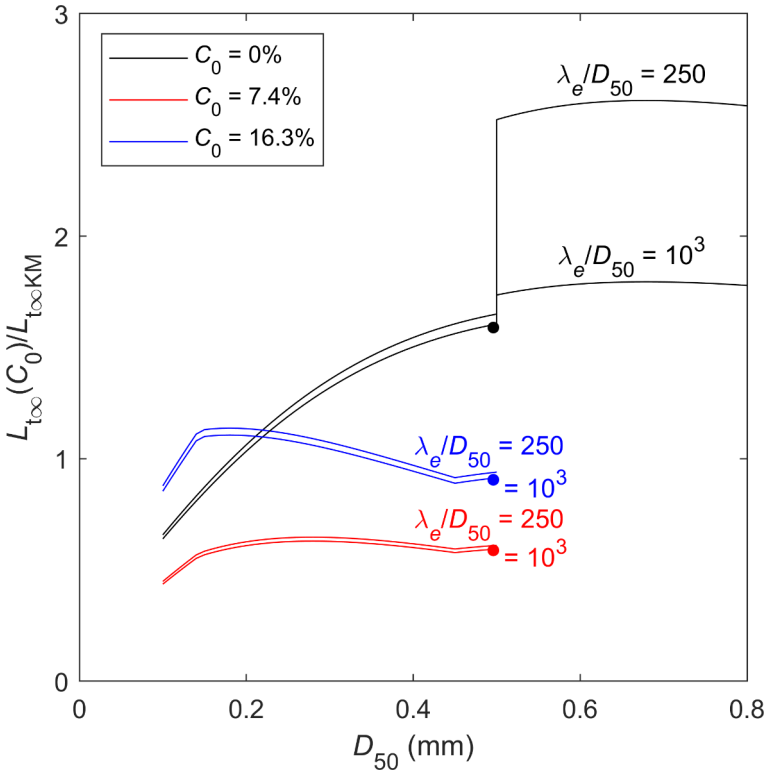

Fig. 3. Relative size of $L_{t\infty}(C_0)$ from Eq. (7b) normalised by the clean-sand $L_{t\infty}$ from Eq. (13), $L_{t\infty KM}$, for $C_0 = 0$, 7.4 and 16.3%. $\lambda_e/D_{50} = 250$ and 1000, and the dots correspond to the Wu et al.[11] clean-sand experiment in Fig. 2a.

Conclusions

Preserved sedimentary bedforms provide important information for reconstructing past hydraulics in subaqueous environments by inverting bedform predictors, but this is usually based exclusively on non-cohesive sand. The present work incorporates the effects of sand-clay mixtures on bedforms, using the experimental results of Wu et al.[13] in the non-cohesive inversion method of Diem[14] for waves alone. Based on wave breaking and threshold of motion limitations, the Diem[14] approach results in ranges for wave conditions. Here we have shown that the inclusion of as little as 7.4% clay in the most extreme case of coarse sand, $D_{50} \geq 0.45$ mm, reduces the possible ranges of water-surface wavelengths and water depths by factors of 3 and 4, respectively. For fine sand, the ranges are reduced by a factor of two. In short, not accounting for the modifying effect of clay in ripple growth and equilibrium geometries, may lead to underestimating the prevailing wave conditions if clay is present.

Methods

Derivation of the Diem[14] approach

For linear wave theory, the dispersion relation and the wave-velocity amplitude, U_0, are

$$\sigma^2 = gk \tanh kh, \tag{8a}$$

$$U_0 = \pi d_0/T, \tag{8b}$$

where $\sigma = 2\pi/T$, $d_0 = H/\sinh kh$ and $k = 2\pi/L$. The wave properties, characterised by equations (8a, b), are subject to two constraints: threshold of motion and wave breaking. For sediment movement $U_0^2 > U_t^2$, where U_t is the threshold wave-velocity amplitude to be determined below, which when combined with equations (8a, b) gives $x < \tanh kh$, Eq. (1a), where $x = L/L_{t\infty}$ and $L_{t\infty} = \pi g(d_0/U_t)^2/2$. The wave-breaking criterion[36] defines the maximum possible wave steepness as, $H/L \leq 0.142 \tanh kh$, which when combined with d_0 and $L_{t\infty}$ gives $x \geq A \cosh kh$, Eq. (1b), where $A = d_0/0.142L_{t\infty}$. It will be shown below, that $A < 1/2$, so if $A = (U_t/U_m)^2/2$, where $U_m = (0.0355\pi g d_0)^{1/2}$ is the maximum wave-velocity amplitude ($U_m > U_t$), then $U_t < U_0 \leq U_m$ and from Eq. (8b) $\pi d_0/U_m \leq T < \pi d_0/U_t$.

The limits of the possible values of x can be found by combining Eqs. (1a, b) using the identity $1 - \tanh^2 kh = \mathrm{sech}^2 kh$, such that the maximum and minimum in x satisfy the equation $x^4 - x^2 + A^2 = 0$, so that $x_{max,\,min}$ are

$$x_{\max,\min} = [1/2 \pm (1 - 4A^2)^{1/2}/2]^{1/2}, \tag{9}$$

where $A < 1/2$, for there to be two distinct values. Here, x and kh are in the ranges $x_{min} \le x < x_{max}$ and $\text{arctanh}x < kh \le \text{arccosh}(x/A)$, respectively. In Fig. 1, for the limiting $A = 1/2$ ($U_m{}^2 = U_t{}^2$) single-valued case the dot corresponds to $x = 2^{-1/2}$, from Eq. (9), and $kh = \text{arctanh}2^{-1/2} \sim 0.88$. Likewise, in the $A = 1/4$ ($U_m{}^2 = 2U_t{}^2$) case the dots mark $x_{max,\,min} = (2 \pm 3^{1/2})^{1/2}/2 \sim 0.97$, 0.26 and $kh_{max,\,min} = \text{arctanh}(x_{max,\,min})$.

Determination of $U_t{}^2$ based on Soulsby[28]

According to Soulsby[28], the Shields parameter for the critical threshold of motion of clean sand is

$$\theta_0 = \frac{0.3}{1 + 1.2D_*} + 0.055(1 - \mathrm{e}^{-0.02D_*}), \tag{10}$$

where $D_* = [(s-1)g/\nu^2]^{1/3}D_{50}$, $s = \rho_s/\rho$, ρ_s and ρ are the sediment and water densities and ν is the kinematic viscosity (~ 1 mm^2 s^{-1}). For waves, $\theta_0 = f_w U_t^2/2(s-1)gD_{50}$, where $f_w = 1.39(6d_0/D_{50})^{-0.52}$ is the skin friction factor[37]. Rearranging the θ_0 wave expression gives U_t^2 as

$$U_t{}^2 = B(g{d_0}^{0.52}D_{50}^{0.48}), \tag{11}$$

where $B = 6^{0.52}(s-1)\theta_0/0.695 = 3.653(s-1)\theta_0$. Equation (11) can be compared with Eq. (12).

Diem[14] threshold of motion constraint

Diem[14] used the Komar & Miller[29] expression for U_t^2, namely

$$U_t{}^2 = (s-1)gd_0 \times \begin{cases} 0.21(d_0/D_{50})^{-0.5}, & D_{50} < 0.5 \text{ mm}, \\ 0.46\pi(d_0/D_{50})^{-0.75}, & D_{50} \geqslant 0.5 \text{ mm}, \end{cases} \tag{12}$$

such that with the inclusion of clay $L_{t\infty} = \pi g{d_0}^2/2B_\theta U_t^2$, $d_0 = \lambda_e/\alpha$ and B_θ and α are given by Eqs. (5) and (6), giving $L_{t\infty}$ as

$$L_{t\infty} = \frac{\pi\lambda_e}{2(s-1)} \times \begin{cases} \frac{1}{0.21[B_\theta \alpha^{1.5}]}\left(\frac{\lambda_e}{D_{50}}\right)^{0.5}, & D_{50} < 0.5 \text{ mm}, \\ \frac{1}{0.46\pi[B_\theta \alpha^{1.75}]}\left(\frac{\lambda_e}{D_{50}}\right)^{0.75}, & D_{50} \geqslant 0.5 \text{ mm}, \end{cases} \tag{13}$$

and $AL_{t\infty}$ as $\lambda_e/0.142[\alpha]$ remains the same. Figure 4 shows the effect of this parameterisation of the threshold of motion for the first example case of Wu et al.[11] depicted in Fig. 2a, d. Unlike Fig. 2d, the measured values of h and L are outside the range predicted for $C_0 = 7.4\%$.

Using the Sleath[21] expression to predict d_0/λ_e

This section considers the effect of using the Sleath[21] expression for d_0/λ_e when $\lambda_e \geq 200$ mm and applies it to the three examples considered in the "Results" section for the clean-sand case. In the clean-sand case, according to Diem[14], d_0/λ_e can be expressed as

$$\frac{d_0}{\lambda_e} = \begin{cases} \alpha_0^{-1}, & \lambda_e < 200 \text{ mm}, \\ 0.778{R_s}^{0.151}, & \lambda_e \geqslant 200 \text{ mm}, \end{cases} \tag{14}$$

where α_0 was taken to be 0.65, but here is 0.61, see Eq. (6), and $R_s = (U_0 d_0/2\nu)^{1/2}$. If $\lambda_e < 200$ mm, then $\alpha_0{}^{-1}\lambda_e$ can be substituted for d_0, as explained in the main paper. However, for $\lambda_e \geq 200$ mm, since the d_0/λ_e ratio can change, Diem[14] showed that an additional step in the calculation was required. The wave-velocity amplitude must still be

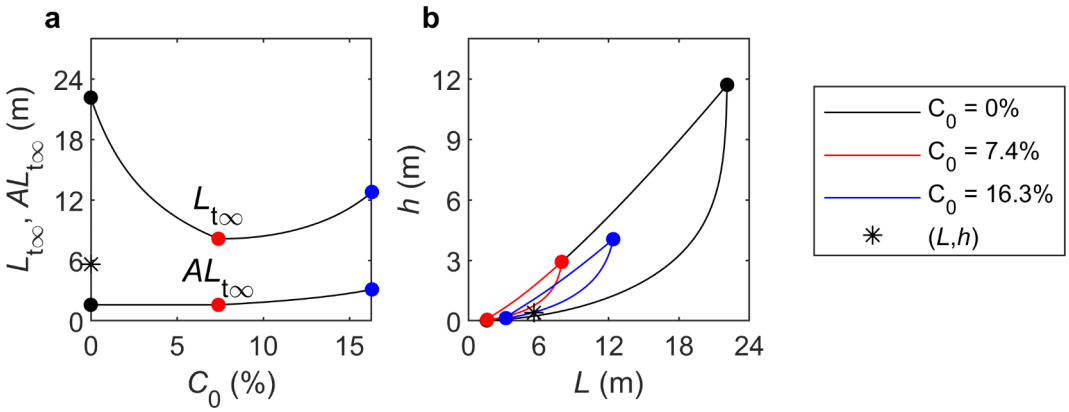

Fig. 4. (**a**) Threshold, $L_{t\infty}$, and wave-breaking scales, $AL_{t\infty}$, Eqs. (13) and (7c), versus C_0 and (**b**) L–h phase space from Eq. (2) showing the different ranges for $C_0 = 0$, 7.4 and 16.3% and the measured h and L for Wu et al.[11], $\lambda_e = 278D_{50}$, $D_{50} = 0.496$ mm, $h = 0.6$ m and $L = 5.62$ m.

Data	D_{50} (mm)	λ_e (mm)	d_0/λ_e (–)	θ_0 (–)	$(d_0/\lambda_e)_{min}$ (–)	$(d_0/\lambda_e)_{max}$ (–)	$L_{t\infty R}$ (–)	$AL_{t\infty R}$ (–)
Wu et al.[11]	0.496	138	1.64	0.032	1.04	1.79	0.51	1.09
Doucette[32]	0.22	250	3.16	0.045	1.07	1.94	0.53	1.18
Boyd et al.[33]	0.11	180	1.74	0.076	1.07	1.86	0.53	1.13

Table 1. Measured D_{50}, λ_e and d_0/λ_e and predicted θ_0 from Eq. (10), $(d_0/\lambda_e)_{min}$ and $(d_0/\lambda_e)_{max}$ from Eq. (15), $L_{t\infty R} = [0.61(d_0/\lambda_e)_{min}]^{1.48}$ and $AL_{t\infty R} = 0.61(d_0/\lambda_e)_{max}$, based on Eqs. (16a, b) and (4b, c) for the three example cases.

in the range $U_t < U_0 \leq U_m$, so that R_s is in the range $(U_t d_0/2\nu)^{1/2} < R_s \leq (U_m d_0/2\nu)^{1/2}$, and therefore from Eq. (14), for $\lambda_e \geq 200$ mm, d_0/λ_e must be in the range $0.778(U_t d_0/2\nu)^{0.0755} < d_0/\lambda_e \leq 0.778(U_m d_0/2\nu)^{0.0755}$. From Eq. (11), $U_t = (Bg)^{0.5} d_0^{0.26} D_{50}^{0.24}$, where $B = 3.653(s-1)\theta_0$, and $U_m = (0.0355\pi g d_0)^{0.5}$, so that the d_0/λ_e range is

$$P_1 \left(\frac{g^{0.5} {d_0}^{1.26} D_{50}^{0.24}}{\nu} \right)^{0.0755} < \frac{d_0}{\lambda_e} \leqslant P_2 \left(\frac{g {d_0}^3}{\nu^2} \right)^{0.03775}, \tag{15}$$

where $P_1 = 0.778(B/4)^{0.03775}$, $P_2 = 0.778(0.0355\pi/4)^{0.03775}$, and the minimum and maximum in the d_0/λ_e range correspond to the threshold of motion and wave breaking, respectively. For a given measured λ_e, the solution to Eq. (15) requires an iteration starting from $d_0 = \alpha_0^{-1}\lambda_e = 1.64\lambda_e$. Substituting $\lambda_e(d_0/\lambda_e)_{min}$ and $\lambda_e(d_0/\lambda_e)_{max}$, from Eq. (15), into equations (4a, b,c) allows the threshold of motion and wave breaking scales, $L_{t\infty}$ and $AL_{t\infty}$, to be expressed as

$$L_{t\infty} = \frac{\pi \lambda_e (d_0/\lambda_e)_{min}^{1.48}}{2B} \left(\frac{\lambda_e}{D_{50}} \right)^{0.48} \tag{16a}$$

$$AL_{t\infty} = \frac{\lambda_e (d_0/\lambda_e)_{max}}{0.142}. \tag{16b}$$

For each of the three example cases considered in the "Results" section, $(d_0/\lambda_e)_{min}$ and $(d_0/\lambda_e)_{max}$ are listed in Table 1, even though the $\lambda_e \geq 200$ mm condition is only met in the Doucette[32] case. In all three example cases, $d_0/\lambda_e = 1.64$ lies between $(d_0/\lambda_e)_{min}$ and $(d_0/\lambda_e)_{max}$. The observed and predicted d_0/λ_e are in close agreement, apart from the Doucette[32] case, where both the d_0/λ_e range from Eq. (15) and $d_0/\lambda_e = 1.64$ underpredict by approximately a factor of two. The values of $L_{t\infty R}$ and $AL_{t\infty R}$ from Eqs. (16a, b) and (4b, c) are also given in Table 1. Since these values for $L_{t\infty R}$ and $AL_{t\infty R}$ are largely similar in all three cases, this suggests that using the orbital approximation $d_0/\lambda_e = 1.64$ for the Doucette[32] case is reasonable, even though $\lambda_e \geq 200$ mm.

Data availability

All data generated or analysed during this study are included in this published article.

Received: 14 June 2024; Accepted: 4 November 2024
Published online: 28 December 2024

References

1. Collinson, J. & Mountney, N. *Sedimentary Structures* (Dunedin Academic, 2019).
2. Vignaga, E. et al. Erosion of biofilm-bound fluvial sediments. *Nat. Geosci.* **6**, 770–774 (2013).
3. Wiberg, P. L. & Harris, C. K. Ripple geometry in wave-dominated environments. *J. Geophys. Res.* **99**, 775–789 (1994).
4. Baas, J. H. A flume study on the development and equilibrium morphology of current ripples in very fine sand. *Sedimentology*. **41**, 185–209 (1994).
5. Perron, J. T., Myrow, P. M., Huppert, K. L., Koss, A. R. & Wickert, A. D. Ancient record of changing flows from wave ripple defects. *Geology*. **46**, 875–878 (2018).
6. Cuadrado, D. G. Geobiological model of ripple genesis and preservation in a heterolithic sedimentary sequence for a supratidal area. *Sedimentology*. **67**, 2747–2763 (2020).
7. Allen, P. A. Some guidelines in reconstructing ancient sea conditions from wave ripplemarks. *Mar. Geol.* **43**, 59–67 (1981).
8. Davies, N. S., Liu, A. G., Gibling, M. R. & Miller, R. F. Resolving MISS conceptions and misconceptions: A geological approach to sedimentary surface textures generated by microbial and abiotic processes. *Earth Sci. Rev.* **154**, 210–246 (2016).
9. Malarkey, J. et al. The pervasive role of biological cohesion in bedform development. *Nat. Commun.* **6**, 6257. https://doi.org/10.1038/ncomms7257 (2015).
10. Parsons, D. R. et al. The role of biophysical cohesion on subaqueous bed form size. *Geophys. Res. Lett.* **43**, 1566–1573 (2016).
11. Wu, X. et al. Wave ripple development on mixed clay–sand substrates: Effects of clay winnowing and armoring. *J. Geophys. Res. Earth Surf.* **123**, 2784–2801 (2018).
12. Wu, X., Fernández, R., Baas, J. H., Malarkey, J. & Parsons, D. R. Discontinuity in equilibrium wave–current ripple size and shape and deep cleaning associated with cohesive sand–clay beds. *J. Geophys. Res. Earth Surf.* **127**, e2022JF006771 (2022). https://doi.org/10.1029/2022JF006771
13. Wu, X. et al. Influence of cohesive clay on wave-current ripple dynamics captured in a 3D phase diagram. *Earth Surf. Dyn.* **12**, 231–247 (2024).
14. Diem, B. Analytical method for estimating palaeowave climate and water depth from wave ripple marks. *Sedimentology*. **32**, 705–720 (1985).
15. Aspler, L. B., Chiarenzelli, J. R. & Bursey, T. L. Ripple marks in quartz arenites of the Hurwitz group, Northwest Territories, Canada: Evidence for sedimentation in a vast, early Proterozoic, shallow, fresh-water lake. *J. Sediment. Res.* **A64**, 282–298 (1994).

16. Wetzel, A., Allenbach, R. & Allia, V. Reactivated basement structures affecting the sedimentary facies in a tectonically quiescent epicontinental basin: An example from NW Switzerland. *Sediment. Geol.* **157**, 153–172 (2003).
17. Allen, P. A. & Hoffman, P. F. Extreme winds and waves in the aftermath of a neoproterozoic glaciation. *Nature*. **433**, 123–127 (2005).
18. Pochat, S. & Van Den Driessche, J. Filling sequence in late paleozoic continental basins: A chimera of climate change? A new light shed given by the Graissessac–Lodève basin (SE France). *Palaeogeogr Palaeoclim Palaeoecol*. **302**, 170–186 (2011).
19. Lamb, M. P., Fischer, W. W., Raub, T. D., Perron, J. T. & Myrow, P. M. Origin of giant wave ripples in Snowball Earth cap carbonate. *Geology*. **40**, 827–830 (2012).
20. Miller, M. C. & Komar, P. D. Oscillation sand ripples generated by laboratory apparatus. *J. Sediment. Petrol.* **50**, 173–182 (1980).
21. Sleath, J. F. A. A contribution to the study of vortex ripples. *J. Hydraul Res.* **13**, 315–328 (1975).
22. Vittori, G. & Blondeaux, P. On the prediction of the characteristics of sand ripples at the bottom of sea waves. *Earth Sci. Rev.* **252**, 104753. https://doi.org/10.1016/j.earscirev.2024.104753 (2024).
23. Malarkey, J. & Davies, A. G. A non-iterative procedure for the Wiberg and Harris (1994) oscillatory sand ripple predictor. *J. Coast Res.* **19**, 738–739 (2003).
24. Mogridge, G. R., Davies, M. H. & Willis, D. H. Geometry prediction for wave-generated bedforms. *Coast Eng.* **22**, 255–286 (1994).
25. Pedocchi, F. & García, M. H. Ripple morphology under oscillatory flow: 2. Experiments. *J. Geophys. Res.* **114**, C12015. https://doi.org/10.1029/2009JC005356 (2009).
26. Tanaka, H. & Dang, V. T. Geometry of sand ripples due to combined wave-current flows. *J. Waterway Port Coast Ocean. Eng.* **122**, 298–300 (1996).
27. Lacy, J. R., Rubin, D. M., Ikeda, H., Mokudai, K. & Hanes, D. M. Bed forms created by simulated waves and currents in a large flume. *J. Geophys. Res.* **112**, C10018. https://doi.org/10.1029/2006JC003942 (2007).
28. Soulsby, R. *Dynamics of Marine Sands: A Manual for Practical Applications* (Thomas Telford, 1997).
29. Komar, P. D. & Miller, M. C. The threshold of sediment movement under oscillatory water waves. *J. Sediment. Petrol.* **43**, 1101–1110 (1973).
30. Whitehouse, R., Soulsby, R., Roberts, W. & Mitchener, H. *Dynamics of Estuarine Muds: A Manual for Practical Applications* (Thomas Telford, 2000).
31. Baas, J. H. et al. Current- and wave-generated bedforms on mixed sand-clay intertidal flats: A new bedform phase diagram and implications for bed roughness and preservation potential. *Front. Earth Sci.* **9**, 747567. https://doi.org/10.3389/feart.2021.747567 (2021).
32. Doucette, J. S. The distribution of nearshore bedforms and effects on sand suspension on low-energy, micro-tidal beaches in Southwestern Australia. *Mar. Geol.* **165**, 41–61 (2000).
33. Boyd, R., Forbes, D. L. & Heffler, D. E. Time-sequence observations of wave-formed sand ripples on an ocean shoreface. *Sedimentology*. **35**, 449–464 (1988).
34. Jago, C. F., Ishak, A. K., Jones, S. E., Goff, M. R. G. & Wales, S. W. An ephemeral turbidity maximum generated by resuspension of organic-rich matter in a macrotidal estuary, *Estuaries Coasts* **29**, 197–208 (2006).
35. Baas, J. H. et al. Integrating field and laboratory approaches for ripple development in mixed sand-clay-EPS. *Sedimentology*. **66**, 2749–2768 (2019).
36. Miche, R. Mouvements Ondulatoires De La mer en profondeur constante ou décroissante. *Ann. Des. Ponts et Chaussées*. **19**, 369–406 (1944).
37. Soulsby, R. L. et al. Wave–current interactions within and outside the bottom boundary layer. *Coast Eng.* **21**, 41–69 (1993).

Acknowledgements

The participation of JM, EMP, XW, RF, JHB and DRP was made possible thanks to funding by the European Research Council under the European Union's Horizon 2020 research and innovation program (grant no. 725955). Participation of RF was also supported by the Leverhulme Trust, Leverhulme Early Career Researcher Fellowship (grant ECF-2020-679).

Author contributions

EMP and RF came up with the concept, based on the experiments undertaken by XW and RF, with assistance from JM in the synthesis. DRP provided the funding for the experiments. JM undertook the analysis and wrote the paper. All authors reviewed the manuscript.

Declarations

Competing interests

The authors declare no competing interests.

Additional information

Correspondence and requests for materials should be addressed to J.M.

Reprints and permissions information is available at www.nature.com/reprints.

Publisher's note Springer Nature remains neutral with regard to jurisdictional claims in published maps and institutional affiliations.

Open Access This article is licensed under a Creative Commons Attribution 4.0 International License, which permits use, sharing, adaptation, distribution and reproduction in any medium or format, as long as you give appropriate credit to the original author(s) and the source, provide a link to the Creative Commons licence, and indicate if changes were made. The images or other third party material in this article are included in the article's Creative Commons licence, unless indicated otherwise in a credit line to the material. If material is not included in the article's Creative Commons licence and your intended use is not permitted by statutory regulation or exceeds the permitted use, you will need to obtain permission directly from the copyright holder. To view a copy of this licence, visit http://creativecommons.org/licenses/by/4.0/.

© The Author(s) 2024